

Interaction Forces of Soft Fiber Reinforced Bending Actuators

Zheng Wang, *Senior Member, IEEE, Member, ASME*, Panagiotis Polygerinos, *Member, IEEE/ASME*, Johannes T. B. Overvelde, Kevin C. Galloway, Katia Bertoldi and Conor J. Walsh, *Member, IEEE*

Abstract—Soft bending actuators are inherently compliant, compact, and lightweight. They are preferable candidates over rigid actuators for robotic applications ranging from physical human interaction to delicate object manipulation. However, characterizing and predicting their behaviors are challenging due to the material nonlinearities and the complex motions they can produce. This paper investigates a soft bending actuator design that uses a single air chamber and fiber reinforcements. Additionally, the actuator design incorporates a sensing layer to enable real-time bending angle measurement for analysis and control. In order to study the bending and force exertion characteristics when interacting with the environment, a quasi-static analytical model is developed based on the bending moments generated from the applied internal pressure and stretches of the soft materials. Comparatively, a finite-element method model is created for the same actuator design. Both the analytical model and the finite-element model are used in the fiber reinforcement analysis and the validation experiments with fabricated actuators. The experimental results demonstrate that the analytical model captures the relationships of supplied air pressure, actuator bending angle, and interaction force at the actuator tip. Moreover, it is shown that an off-the-shelf bend angle sensor integrated to the actuator in this study could provide real-time force estimation, thus eliminating the need for a force sensor.

Index Terms—soft robot, bending, fluidic actuator, modeling, interaction force.

I. INTRODUCTION

RIGID robots with motor-driven actuators rely on sensory feedback and control to achieve the compliance required for physically interacting with humans and handling unstructured or delicate objects [1, 2]. However, soft robots [3-

Z. Wang* is with the Department of Mechanical Engineering, The University of Hong Kong, Hong Kong, China (email: zheng.wang@ieee.org).

P. Polygerinos is with the Ira A. Fulton Schools of Engineering at Arizona State University, ASU at the Polytechnic School, 6075 S. Innovation Way W. Mesa, AZ 85212 (email: polygerinos@asu.edu).

K. C. Galloway is with School of Engineering at Vanderbilt University, 2400 Highland Avenue, Nashville, TN 37215, USA (email: kevin.c.galloway@vanderbilt.edu).

J. T. B. Overvelde and K. Bertoldi* are with the School of Applied Sciences and Engineering & the Kavli Institute for Bionano Science and Technology, Harvard University, 29 Oxford Street, Cambridge, MA 02138, USA (e-mail: overvelde@seas.harvard.edu; bertoldi@seas.harvard.edu).

C. J. Walsh* is with the School of Applied Sciences and Engineering & the Wyss Institute at Harvard University, 60 Oxford Street, Cambridge, MA 02138, USA (email: walsh@seas.harvard.edu).

*Corresponding author(s).

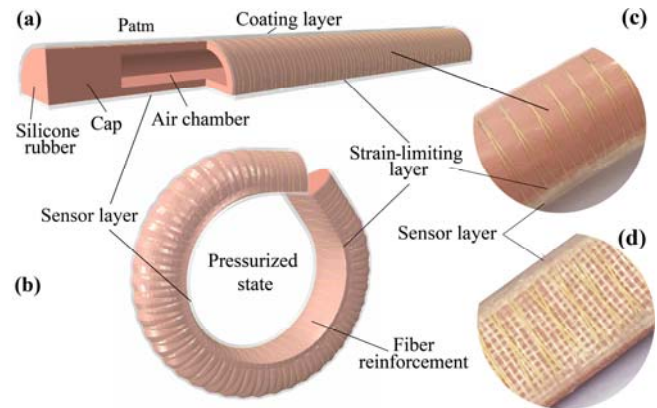


Fig. 1. Structure and bending motion of soft bending actuator. (a) unactuated; (b) fully pressurized; (c) top wall details; (d) bottom layer details.

5] provide an alternative approach due to their inherent compliance and back-drivability with compact and lightweight mechanical structures [6]. The fluidic actuation media (pneumatics or hydraulics) provides unique characteristics comparing with electric motors [7-10]. Piezoelectric robotic actuators could also achieve compliance, but their application are more towards high precision micromanipulation due to their limited range of motion and force capabilities [11-14]. The most widely used soft actuator is the pneumatic artificial muscle (PAM) that generates linear contraction with pressurization. Applications of PAMs range from biocompatible devices [15], to humanoid robots [16, 17], and compliant manipulators [18]. Modeling and control of PAMs have been investigated extensively in the literature [19-21]. However, in order to create bending motions, most robotic applications use PAMs to drive mechanisms consisting of rigid links and joints [16, 18]. Therefore despite the compliance of PAMs, the compliance of the overall robotic systems has often been limited by the rigid components.

It has previously been shown that soft bending actuators can generate inherent bending motion without requiring any rigid components [22-24]. They are constructed from polymeric [24] or a combination of elastomeric (hyper-elastic silicones) and inextensible materials (fabrics and fibers) [22, 23] and activated by pressurizing fluid. There are various designs for soft bending actuators. A single-chamber design is shown in Fig. 1, where bending is created by asymmetrically constraining the extension of an air chamber [25, 26] with different choices for the cross sectional shape, such as circular [27, 28], rectangular

[29], or hemi-circular [23, 30]. There are also reported designs of multi-chamber actuators for more complex motions [31-34], or combined opposing chambers that achieve flexing and extending motions [30,35]. To achieve higher dexterity, a multi degree-of-freedom (DOF) actuator could consist of several small single-chamber bending actuator segments [27, 36]. Furthermore, different actuator designs have been reported for biomimetic systems [30-32], safe and compliant actuators [35, 37], and delicate manipulators [25, 26, 27].

Modeling the behavior of soft bending actuators is challenging due to the material nonlinearity and the large deformations they produce. Most prior works on modeling soft bending actuators were focused on the quasi-static behaviors, in which the actuators undergo motions slow enough, such that no dynamic effects (transients, visco-elasticity of soft material, etc) were considered. Most previous works followed an empirical approach [28, 38, 39], while some reported using the finite-element method (FEM) [24, 30]. In particular, analysis of their force exertion ability when interacting with the environment was not reported previously. Regarding actuator dynamics, recent work investigated the actuation speed and hysteresis in a multi-chamber soft bending actuator design [34].

In the authors' previous work, a quasi-stationary analytical model accounting for large deformations was developed for a soft bending actuator with fiber reinforcements. The model was successful in capturing the relationship between input pressure and actuator angle. In addition, multiple candidates for the actuator designs were compared, revealing that the hemi-circular cross sectional shape required the lowest pressure to bend to the same angle [40].

In this study, the quasi-static behavioral characteristics of a soft bending actuator with fiber reinforcement and integrated sensing is investigated. After presenting the actuator design in Section II, the influence of the fiber reinforcement layer on actuator motion is investigated for the first time in Section III, using both an analytical model and a FEM model created for the same actuator design, showing that with sufficiently low pitch angle, the fiber layer could be regarded as radial constraint instead of a variable with actuator motion. On this basis, characterizations of the bending actuator motion and forces were carried out in Section IV, where a bending sensor is integrated into the actuator design, and the analytical model previously derived for free-space bending in [40] is extended to incorporate the bending sensor, and characterize both actuator bending and tip force exertion during interactions. The newly derived analytical model has low computational cost and is capable of predicting interaction forces at the actuator tip without using a force sensor. The performance of the proposed models is validated in Section V, with experiments using fabricated actuators.

II. ACTUATOR DESIGN

This study is focused on the actuator design shown in Fig. 1, previously proposed in our earlier works [10, 22, 40], which consists of a single stretchable chamber with hemi-circular cross section, a strain-limiting layer, a reinforcement fiber layer encircling the chamber to constrain radial expansion during pressurization, and a sensor layer below the strain-limiting layer for bending angle measurements. The actuator chamber and the

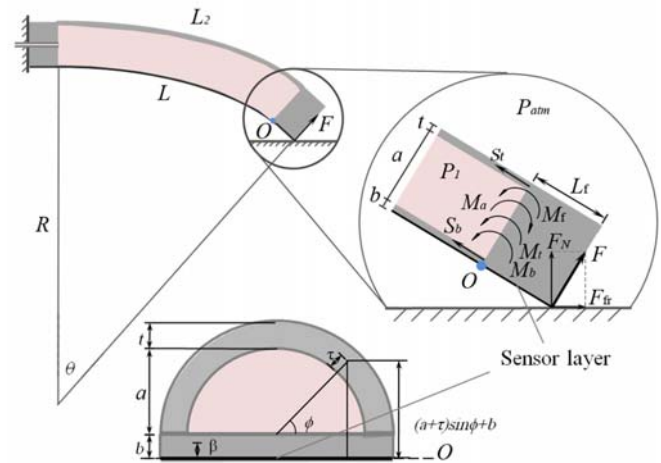


Fig. 2. Actuator bending with the cross-sectional view and the torque equilibrium of the distal tip. The proximal tip of the actuator is fixed and the distal tip is in contact with an object.

sensor layer are fabricated using hyperelastic material, while the strain-limiting layer and fiber reinforcement layer are made from flexible but inextensible materials. With the actuator motion generated by soft material stretch, such actuator design could achieve smooth and continuous bending motion from its natural resting position to around 360 degrees, with resolutions subject to the supplied air pressure.

The forces and geometric parameters necessary for deriving the force model are illustrated in Fig. 2. The actuator has a hemi-cylindrical top wall with an inner radius a and thickness t , a flat rectangular bottom layer of thickness b and width $2(a + t)$, and an initial length of L . The sensor layer at the bottom of the actuator has a pocket throughout its length to accommodate a thin flexible bend sensor that measures the bending angle θ . When the air chamber is pressurized ($P_1 > P_{atm}$), the top wall extends while the bottom layer is constrained by the inextensible strain-limiting layer. Therefore the actuator bends towards the bottom layer with a radius R and angle θ . With its proximal tip firmly mounted, the actuator will exert a force F if the distal tip is in contact with an external object, which could be decomposed into a normal force F_N perpendicular to the contact surface, and a frictional force F_{fr} parallel to the contact surface. The combined interaction force F is perpendicular to the bottom layer to ensure a constant bending moment arm of L_f with respect to the fulcrum O .

III. EFFECT OF FIBERS

The fiber reinforcement layer in the actuator design constrains the natural expansion of the actuator chamber during pressurization and plays an essential role in generating the bending motion of the actuator. Assuming fiber inextensibility, the fiber pitch (i.e. density of winding) is an essential variable to be considered in actuator design. For linear PAMs, change of fiber pitch is part of the fundamental motion creation mechanism, hence it must be considered in PAM design and modeling. However, for bending soft actuators, there is no analysis on how fiber pitch contributes to actuator motion, or guideline available on how to choose the fiber pitch for actuator design. Therefore, we first investigate the relations between fiber pitch, actuator bending, and actuator deformation, to

reveal that unlike PAMs, the fiber pitch is not a variable involved in the actuator bending. Moreover, the conditions are derived, where pitch angle can be ignored and the fiber layer becomes a constraint to actuator motions.

A. Analytical study

First, we investigate the effect of the reinforcement fiber analytically. As shown in Fig. 1, the fiber layer consists of a left-handed helical fiber winding encircling the actuator body for n times, and an opposing symmetrical right-handed winding to balance out potential twisting effects. Therefore, for a given actuator design (diameter, wall thickness, and length), the arrangement of the fibers is fully determined by the pitch of the helix. In fact, the pitch angle φ determines the fiber turn number n for a given actuator length, and affects the ability of the fiber layer to constrain the actuator geometry under pressurization.

For simplicity the actuator is regarded as a hemi cylinder with diameter $u_0 = 2(a + t)$, combining both the top and the bottom layers enclosed by the fiber. Fig.3 shows a segment of the unpressurized actuator, with all parameters needed to fully define its geometry (note that for the sake of clarity only the left-hand winding fiber is shown). The length of the bottom layer of the corresponding actuator segment v_0 , is a function of the fiber turn number n and the actuator length L :

$$v_0 = \frac{L}{2n}. \quad (3.1)$$

Here v_0 is an invariant term during actuator deformation, since the inextensible bottom layer prevents the bottom layer from any expansion. The top actuator wall, however, is not subject to this constraint and hence could extend beyond its original length of v_0 . In addition, the fiber segment is also assumed to be inextensible with a uniform curvature. Therefore, for the unpressurized actuator segment, the relationship for the fiber length w_0 , the radius σ_{w0} , the arc angle $2\psi_{w0}$, and the pitch φ are:

$$\begin{aligned} \sin\psi_{w0} &= \frac{\sqrt{v_0^2 + u_0^2}}{2\sigma_{w0}}, \cos\psi_{w0} = \frac{\sigma_{w0} - h_0}{\sigma_{w0}}, w_0 = 2\psi_{w0}\sigma_{w0}, \\ \sin\varphi_0 &= \frac{v_0}{\sqrt{v_0^2 + u_0^2}} = \frac{v_0}{2\sigma_{w0}\sin\psi_{w0}}. \end{aligned} \quad (3.2)$$

After the actuator is pressurized, most of the above will not hold due to the bending of the bottom layer. To simplify the analysis, here we assume the bottom layer only bends longitudinally with the actuator and ignore any lateral bending or bulging, as shown in Fig. 3(c). Hence the width of the actuator remains constant while the height of the hemi cylinder h changes as a function of the bending angle θ .

When the actuator is pressurized (Fig. 3(c)), the bottom layer length v_0 , diameter u_0 , and the fiber length w_0 remain constant, due to the inextensibilities of the strain-limiting layer and the reinforcement fiber. All other variables ($\sigma_w, h, \varphi, \psi_w$) instead change as a function of the applied pressure (see Fig. 3(c)) and their values in the deformed configuration are denoted with ($\sigma_w, h, \varphi, \psi_w$). Denoting with θ the overall actuator bending angle (see Fig. 2), the angle ψ_v spanned by the considered segment (Fig. 3(d)) is given by

$$\psi_v = \frac{\theta}{2n}. \quad (3.3)$$

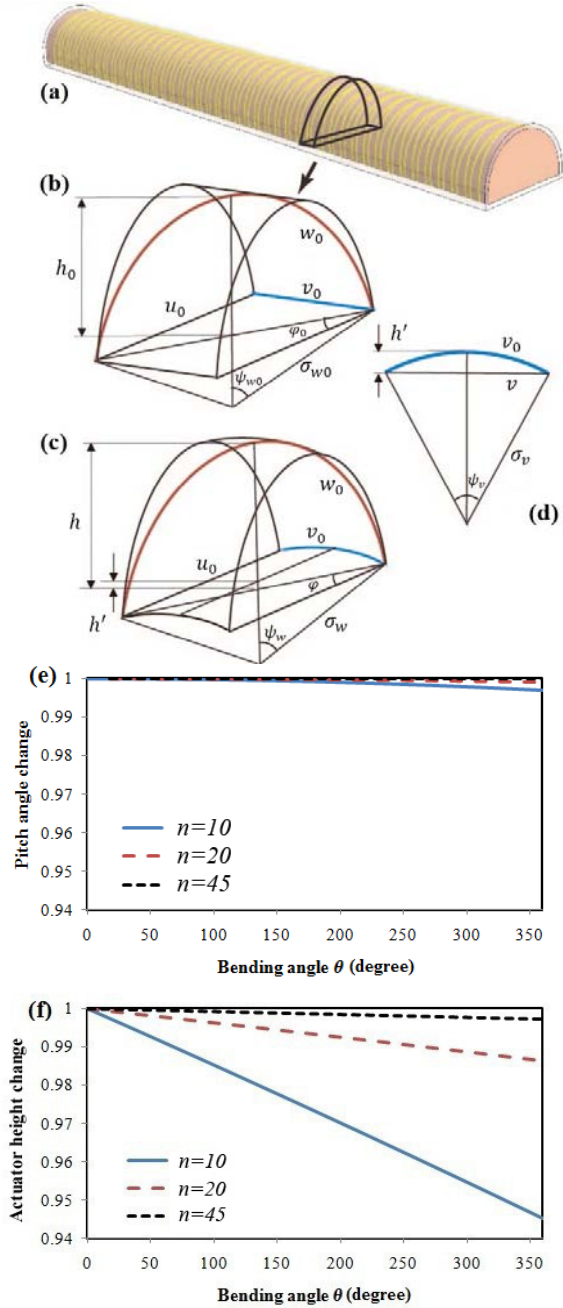


Fig. 3. Pitch angle analysis. (a) a segment of the actuator containing one turn of fiber, (b) the un-pressurized actuator section, (c) same section pressurized, (d) bottom layer side view, (e) Effect of actuator bending angle θ on the fiber pitch angle φ_0/φ for an actuator design with $(a, b, t, L) = (6, 2, 2, 170)$ mm, (f) Effect of actuator bending angle θ on actuator height, change $(h - h')/h_0$, with the same actuator design.

The parameters $\sigma_w, h, \varphi, \psi_w$ and v (defined in Fig. 3(d)) characterizing the deformed configuration can then be expressed as function of ψ_v, w_0, v_0 , and u_0 using the following geometric relations

$$\begin{aligned} \sin\psi_w &= \frac{\sqrt{v^2 + u_0^2}}{2\sigma_w}, \cos\psi_w = \frac{\sigma_w - h}{\sigma_w}, w_0 = 2\psi_w\sigma_w, \\ \sin\varphi &= \frac{v}{\sqrt{v^2 + u_0^2}} = \frac{v}{2\sigma_w\sin\psi_w}, \sigma_v = \frac{v}{\psi_v}, v = 2\sigma_v\sin\frac{\psi_v}{2} \end{aligned}$$

$$h' = \sigma_w - \sigma_w \cos \frac{\psi_w}{2}. \quad (3.4)$$

where σ_w denotes the radius of curvature of the pressurized actuator (see Fig. 3(d)) and h' is the height of the arch formed by the considered section (see Fig. 3(d)). Combining Eqns. (3.2)-(3.4) we obtain

$$v = \frac{4nv_0}{\theta} \sin \frac{\theta}{4n}, \quad \frac{\sin \psi_w}{\psi_w} = \frac{v}{2\psi_{w0}\sigma_{w0}\sin\varphi}, \quad \sin\varphi = \frac{v}{\sqrt{v^2+u_0^2}},$$

$$h - h' = \frac{\psi_{w0}\sigma_{w0}}{\psi_w} (1 - \cos\psi_w) - \frac{2nv_0}{\theta} (1 - \cos \frac{\theta}{4n}). \quad (3.5)$$

Eq. (3.5) can now be used to determine numerically the effect of the overall actuator bending angle θ on both the fiber pitch angle and actuator height. A series of simulations were carried out on an actuator design of $(a, b, t, L) = (6, 2, 2, 170)$ mm, consistent with the actuators fabricated and used in experiments. In Fig. 3(e) and Fig. 3(f) we report the changes in pitch angle (φ_0/φ) and actuator height ($(h - h')/h_0$) as function of the actuator bending angle θ for $n=10, 20$ and 45 . The results reported in Fig. 3(e) show that the pitch angle changes for all actuator turn numbers are within 1% for the full bending range of 360 degrees. However, the change in actuator height is significant for low fiber turn number (h' decreased by 5.5% at full bending for $n=10$), and becomes negligible for large turn numbers, for instance, $n=20$ (1.4%) and 45 (0.3%).

Two major conclusions could be drawn from the analytical investigation: 1) fiber pitch is not a variable involved in actuator bending. This is fundamentally distinctive from the motion generation mechanism of PAM; 2) the fiber layer defines actuator motion by constraining radial expansion. In particular, to ensure sufficient constraining, a low pitch (or high turn number) is desirable (for the current design, $n>20$ or $\varphi < 20^\circ$).

B. Finite Element Model

To validate the analytical model, a 3D finite element (FE) model of the actuator was created. It was constructed within the nonlinear finite-element code ABAQUS/standard using the Yeoh hyperelastic model [41] and assuming incompressibility for all solid materials. The FE model consisted of an internal hemi-cylinder chamber and an external hemi-cylinder coating layer modeled using solid tetrahedral quadratic hybrid elements (ABAQUS element type C3D10H). The reinforcement fibers were then modeled by quadratic beam elements (ABAQUS element type B32), which were connected to the internal chamber and the coating layer with tie constraints. Here the inextensible layer was not modeled separately, but was combined with the bottom layer for better computational efficiency and increasing simulation convergence. More details on the FE model are provided in our previous work [40].

The FE model was used to study the influence of the fiber reinforcement layer on the change of the actuator shape induced by pressurization and results were compared with the analytical results previously described. Seven different FEM models were created with different number of fiber turns, $n=5, 15, 25, 35, 45, 55,$ and 65 , while keeping the actuator dimensions constant. Each model was pressurized to 90 and 180 degrees in free space and snapshots of the results obtained for $n=5, 15, 45,$ and 65 are shown in Fig. 4(c). For $n=5$ the sparse fiber results in large areas of unconstrained actuator surface between the fiber turns. Therefore, at 90 degrees bending the model presented large

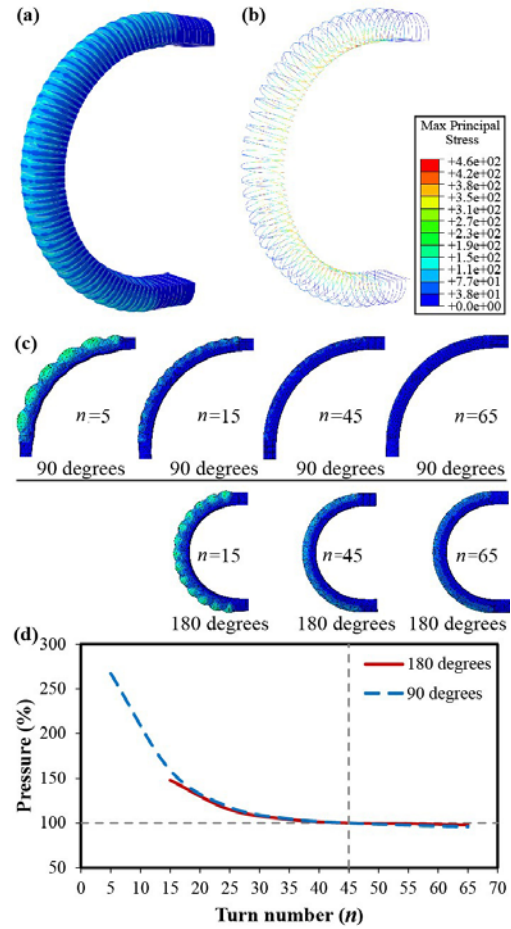


Fig. 4. FEM model of the actuator ($n=45$). (a) pressurized actuator. (b) the reinforcement fiber showing stress concentration at the bottom strain-limiting layer. (c) FEM simulations with turn number of 5, 15, 45, and 65 at 90 and 180 degrees bending. (d): Pressure required to reach 90 and 180 degrees bending for different n , with pressures for $n=45$ taken as references (100%).

nonlinear bulges, while at 180 degrees bending the simulation could not converge due to excessive material deformation and hence ballooning instability. However, as the fiber turn number got higher, the radial expansion quickly decreased and became negligible for $n>35$. In Fig. 4(d) we then report the normalized pressure required to bend the actuator by 90 and 180 degrees as function of n . The pressures required for $n=45$ actuator were taken as the reference (100%) for both 90 (59.4 kPa) and 180 (113.4 kPa) result groups. These results clearly indicate that for $n>35$, the response of the actuator is not affected by the specific number of turns.

C. Comparison of analytical and numerical results

In Fig. 5(a) and Fig. 5(b) we report our analytical and numerical predictions for the evolution of the actuator height h and pitch angle φ as a function of the turn number n for $\theta=0$ and $\theta=360$ degrees. For other angles between 0 and 360 degrees, the results also fell between those of the two angles, therefore they were not shown here. The actuator height h was extracted from the FE simulations as the averaged distance along the length between the top of the actuator and the undeformed bottom layer surface, thus ignoring the bottom layer bulging (as to match the assumption of flat bottom layer in the analytical model). Note that, since FE simulations with $n<15$ were not

able to converge due to ballooning instability, only numerical results for $15 \leq n \leq 65$ are reported.

For the pitch angle, analytical and numerical results agree very well and indicate that pressurization has a negligible effect on φ , regardless of the number of turns n .

Differently, the analytical results reported in Fig. 5(b) show that for small number of fiber turns (i.e. $n < 10$), pressurizing the actuator resulted in a significant deformation in actuator height. However, as the number of fiber turns increased ($n > 20$), the deformation of the cross section rapidly reduced and became negligible. Note that for analytical results, actuator height after bending is smaller than the initial height. This is not contradicting to the bulging observed in FEM results in Fig. 4(c): while the analytical models of (3.5) describes the actuator deformation resulting from the constraining fiber, the bulging of FEM modeling resulted from the unconstrained soft material between the adjacent fibers, which exhibited ballooning expansion despite the constraining fiber was reducing the actuator height. This was verified by the trend of reduced bulging with increasing fiber turn number, such that denser fiber resulted in less surface of unconstrained soft material, hence less bulging. The FE results confirmed that for $n > 20$ the deformation of the actuator height was not affected by the number of fiber turn, but showed that h converged to 6.5mm instead of the 6mm undeformed radius. This discrepancy was probably due to the assumption of constant actuator width, while in reality the actuator bottom layer would bulge with pressurization and therefore increase in height, which would affect the actuator height as well as the structural stiffness.

In summary, both analytical and FE results clearly indicate that fiber pitch is not a variable of actuator bending, and that the fiber layer design does affect the actuator geometry change and hence the bending performance. However, with sufficiently low pitch and high turn number ($\varphi < 20^\circ$, $n > 20$), the fiber layer could simply be regarded as a constraint to actuator radial expansion. Therefore, a reinforcement fiber layer with $n = 45$ ($\varphi = 9^\circ$) was used for the rest of this study.

This conclusion is substantially different from those on the PAM actuators, where the fiber pattern is a defining factor for the actuator performance [20, 21]. This can be justified by the fundamental difference in motion creation between the linear PAM actuator and the bending actuator in this study. For the PAMs, the fibers transform radial expansion into linear contraction and generate actuator movement, therefore the pattern of fiber winding plays a major role in the geometrical transitions during the actuation procedure, hence affecting actuator performance. On the other hand, for the bending actuator in this study, expansion asymmetry is created by the inextensible layer attached to the actuator bottom, not the fiber winding. Instead, a sufficiently dense ($n=45$, $\varphi = 9^\circ$ for the actuator design in this study) fiber layer only serves as a constraint to radial expansion, does not have a critical influence on actuator behavior. The analytical model provides a convenient method to verify this condition for a different actuator design: equation (3.5) could be used based on the actuator geometrical information to decide whether a new fiber turn number is sufficient for negligible actuator height change ($\frac{h-h'}{h_0} < 1\%$) within the desired actuator bending range θ .

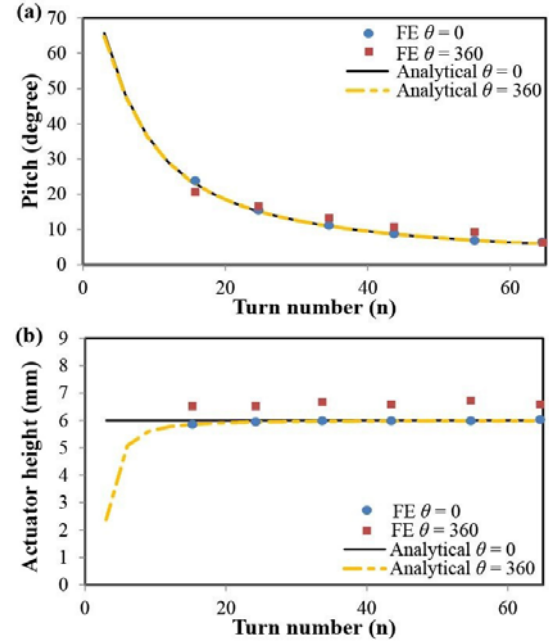


Fig. 5. Fiber analysis comparison with analytical model (Analytical) and Finite Element Analysis (FE). Upper (a): change of fiber pitch φ versus turn number n , for 0 and 360 degrees bending; Lower (b) change of actuator height h versus n , for 0 and 360 degrees bending. (For turn number $n=5$ the FEA simulation did not converge at full bending of 360 degrees, therefore the results are not shown here)

IV. ANALYTICAL MODEL TO PREDICT THE FORCE EXERTED BY THE ACTUATOR

Modeling assumptions. The following assumptions are made regarding the actuation process: i) the radial expansion of the actuator is negligible because of the constraint provided by the fiber reinforcement layer; ii) the supplied air has sufficient flow and the air pressure changes slowly, such that the actuator always reaches steady states; iii) the materials used to fabricate the actuator are incompressible; iv) force interaction, if applicable, only occurs at the actuator tip, and the bending curvature of the actuator is uniform for all bending angles; v) effect of gravity is not considered; vi) the hyper elastic material of the actuator only experiences elastic deformation.

Hyper-elastic material model. Besides the actuator geometry and the actuation process, the stress-strain properties of the hyperelastic materials also need to be considered. The Neo-Hookean (N-H) hyperelastic model [42] is used in this study to capture the response of the hyperelastic material used to fabricate the actuator. Assuming material incompressibility, the strain energy density W is defined as:

$$W = \frac{\mu}{2}(I_1 - 3), \quad (4.1)$$

where μ is the initial shear modulus of the material, I_1 is the first invariant of the three (axial, horizontal, and vertical) principal extension ratios λ_1 , λ_2 , and λ_3 ,

$$I_1 = \lambda_1^2 + \lambda_2^2 + \lambda_3^2. \quad (4.2)$$

The principal nominal stresses s_i can be obtained as [40]:

$$s_i = \frac{\partial W}{\partial \lambda_i} - \frac{p}{\lambda_i}, \quad (4.3)$$

where p is a common Lagrange multiplier for $i=1, 2, 3$. Note that in our model different material properties μ_t , μ_b , and μ_s

are used for the top layer, the bottom layer, and the bend sensor, respectively. We also want to highlight the fact that μ_t and μ_b describe the shear modulus of the entire actuator layer (either top or bottom) consisting of hyperelastic materials, reinforcement fibers, and the strain-limiting layer. The values of μ_t , μ_b , and μ_s are determined empirically through a calibration process as discussed in Section 5.1.

To derive an analytical model that relates the input air pressure and the force exerted by the actuator, we start by noting that the radial expansion of the actuator is constrained by the fiber reinforcement, resulting from the analysis on the fiber layer in Section III, so that the circumferential stretch is approximated to be equal to unity (i.e. $\lambda_2 = 1$). Following a similar derivation procedure as presented in [40], equation (4.3) could be simplified using a unified extension ratio λ , and the axial nominal stress becomes:

$$s_1 = \frac{\partial W}{\partial \lambda_1} - \frac{p}{\lambda_1} = \mu \left(\lambda - \frac{1}{\lambda^3} \right). \quad (4.4)$$

Basic moment equilibrium. Based on the discussions of free-space motion in [40], in this work we extend the moment equilibrium to consider interaction forces at the actuator tip. At each bending configuration, there are four bending moments involved in the bending of the actuator (Fig. 2): M_a is the pressure-induced bending moment generated by the internal air pressure acting on the actuator tip around the pivot point, O ; M_t and M_b are the material stretch moments of the top and bottom layers, respectively (note that M_b also incorporates the moment required to bend the sensor layer); and M_f is the tip force bending moment, exerted by the interaction force applied to the actuator tip if in contact with an external object. Gravity was ignored, as the actuator weight (around 20g overall: 10g for the proximal end connection mechanism, 10g for the rest of the actuator, that is 0.1N gravity for the part actually involved in bending) was significantly smaller than the actuating forces (6N at 100kPa, 15N at 250kPa). While M_a acts clockwise around the fulcrum O , M_t , M_b , and M_f all act counter-clockwise to O . Therefore the following moment equilibrium condition needs to be satisfied:

$$M_a - M_f = M_t + M_b. \quad (4.5)$$

Actuator moment components. To obtain an analytical expression linking the applied pressure to the force exerted by the actuator, we next proceed to obtain explicit relationships for each moment.

1) For the hemi-circular actuator tip with radius a , M_a (see [40]) can be calculated as

$$M_a = \frac{4a^3 + 3\pi a^2 b}{6} P_{in} = V_a P_{in}. \quad (4.6)$$

where $P_{in} = P_1 - P_{atm}$, and

$$V_a = \frac{1}{6}(4a^3 + 3\pi a^2 b). \quad (4.7)$$

2) For the bottom layer, we note that the principal stretch λ is a function of the vertical position. In particular, introducing the coordinate β and the actuator bending radius R as shown in Fig. 2, it can be written as [40]:

$$\lambda = \frac{R+\beta}{R} = \frac{\beta\theta}{L} + 1. \quad (4.8)$$

It follows that

$$M_b = \int_0^b 2s_1(a+t)L\beta d\beta + M_s = 2\mu_b(a+t)L^2\xi(\theta) + M_s, \quad (4.9)$$

where

$$\xi(\theta) = \frac{1}{\theta^2} \left(\frac{\bar{\theta}^3}{3L^3} - \frac{\bar{\theta}^2}{2L^2} + \frac{L}{\bar{\theta}} - \frac{L^2}{2\bar{\theta}^2} - \frac{1}{3} \right), \quad M_s = \mu_s\theta \quad (4.10)$$

and $\bar{\theta} = b\theta + L$. Here we assume the moment M_s required to bend the sensor to be $\mu_s\theta$, a linear function of the actuator bending angle θ , as guided from our experimental results. The value of the sensor stiffness μ_s is determined from calibration.

3) Finally, for the top layer, λ depends on the coordinates ϕ and τ defined in Fig. 2 as [40]:

$$\lambda = \frac{R+b+\sin\phi(a+\tau)}{R}, \quad (4.11)$$

so that

$$M_t = 2 \int_0^t \left(\int_0^{\frac{\pi}{2}} s_1((a+\tau)\sin\phi + b)(a+\tau)L d\phi \right) d\tau. \quad (4.12)$$

Approximation. Different from the polynomial solution of (4.9) for the bottom layer, the integral of (4.12) can only be solved numerically, as shown in [40], which would restrict the application of the model in analysis and real-time calculations.

In this work, we obtain an explicit expression for M_t by replacing the hemi cylinder top wall, with a flat top wall located at a distance $b + \nu(a+t)$ from the bottom of the actuator, ν denoting a coefficient to be determined. With this approximation, λ in (4.11) is simplified and becomes independent from ϕ

$$\lambda = \frac{R+b+\nu(a+t)}{R}. \quad (4.13)$$

Substitution of (4.13) into (4.12), yields

$$\tilde{M}_t = 2\mu_t \cdot \chi_t \cdot \zeta(\theta), \quad (4.14)$$

where

$$\chi_t = \frac{t^3}{3} + \frac{(4a+\pi b)t^2}{4} + \frac{(2a^2+\pi ab)t}{2}, \quad (4.15)$$

and

$$\zeta(\theta) = \frac{L+(b+\nu(a+t))\theta}{L} - \left(\frac{L}{L+(b+\nu(a+t))\theta} \right)^3. \quad (4.16)$$

The numerical value of ν can be determined empirically by comparing the values of M_t for bending angles θ from 0 to 360 degrees using the exact (4.12) and approximate (4.14) expressions for different ν values. For an actuator with $(a, b, t, L) = (6, 2, 2, 170)$ mm, we found that $\nu = 0.65$ yields <5% approximation error for the entire bending range of 0 to 360 degrees. Therefore, (4.14) with $\nu = 0.65$ is used in the rest of this study as a valid approximation of (4.12).

Force model. Finally, assuming that an external object is in contact with the actuator tip as illustrated in Fig. 2, the force F at the tip of the actuator results in an exerted moment M_f ,

$$M_f = L_f \cdot F, \quad (4.17)$$

where L_f denotes the actuator tip length. Note that we implicitly assume that the force interaction happens at the end of the actuator and we do not account for deformation of the actuator tip due to force exertion.

We are now in a position to predict both the bending of the actuator in free space and its force exertion during interaction with an object at the tip. In particular, substituting (4.6), (4.9) and (4.14) into the equilibrium condition (4.5) and assuming

$M_f=0$, the relation between P_{in} and θ for an actuator bending in free space is obtained as

$$P_{in} = \frac{2\mu_b(a+t)L^2\xi(\theta)+2\mu_t\chi_t\zeta(\theta)+\mu_s\theta}{V_a}, \quad (4.18)$$

where $P_{in} = P_1 - P_{atm}$, μ_b , μ_t , and μ_s are material properties for the bottom layer, top wall, and the bend sensor, V_a , $\xi(\theta)$, χ_t , and $\zeta(\theta)$ are given in (4.7), (4.10), (4.15) and (4.16), respectively.

Moreover, if the tip of the actuator is constrained, the following relationship between input pressure, bending angle, and bending force can be obtained from Eq. (4.5)

$$M_f = V_a P_{in} - 2\mu_b(a+t)L^2\xi(\theta) - 2\mu_t\chi_t\zeta(\theta) - \mu_s\theta, \quad (4.19)$$

If both the pressure P_{in} and the bending angle θ can be measured, (4.18) can be used to calculate the interaction force of the actuator both under isotonic (constant pressure) and isometric (constant angle) conditions. Interestingly, since Eq. (4.18) consists of polynomial functions of P_{in} and θ , its right hand side can be calculated easily and it is therefore suitable for real-time applications.

V. EXPERIMENTAL VALIDATION

A. Experimental setup and calibration

The actuators were fabricated using a multi-step molding process with 3D printed molds [22, 40]. A hemi-circular steel rod was used to create the air chamber in the first rubber layer (Elastosil M4601 A/B Wacker Chemie AG). Woven fiberglass (S2-6522 plain weave) was attached to the flat bottom surface using silicone adhesive as the strain limiting layer. Kevlar fiber of 0.38 mm diameter was then hand wound in a double helix pattern around the length of the actuator body. Fiber reinforcements were further secured by placing the entire assembly into another mold to encapsulate the actuator body in a 1.0mm thick silicone layer (Ecoflex-0030 silicone, Smooth-on Inc.). The actuator body was then removed from the steel rod and capped at both ends with silicone (Elastosil M4601 A/B). A vented screw (10-32) was fed through the silicone cap and became the connection for the pneumatic tubes. A sensor layer of 12x170x2mm (Ecoflex-0030, Smooth-on Inc.) was molded separately and attached to the actuator bottom layer with flexible silicone adhesive. The sensor layer had a 6x170mm central pocket for a flexible bend sensor (Spectra Symbol Flex Sensor FS-L-0095-103-ST) of 5x100x1mm. The sensor exhibited very good linearity ($R^2 > 0.99$) between angle and resistance when calibrated with a goniometer. For this study we fabricated actuators of design $(a, b, t, L) = (6, 2, 2, 170)$ mm.

An experimental setup was developed (Fig. 6(b)) with integrated air pressure regulation and force/torque sensing (Nano17, ATI Industrial Automation), which was previously reported in [10, 22]. The proximal tip of the actuator was mounted firmly to the mounting base and connected to the air regulator. As the distal end bends downwards, the overall contact force F on the distal tip (as shown in Fig. 2, F is always perpendicular to the actuator bottom surface) will vary in direction with respect to the horizontal surface. To adapt to the variation of contact direction, an extension bar was attached to the force sensor, the 6-DoF force/torque measurements were

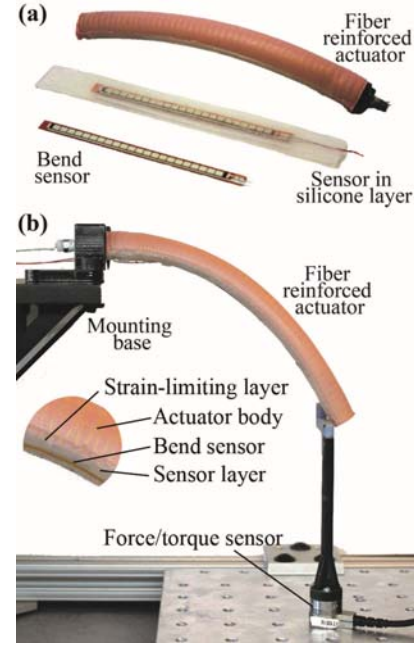


Fig. 6. Experimental setup. (a) sensorized actuator (b) evaluation platform with actuator mounting base and force/torque sensor.

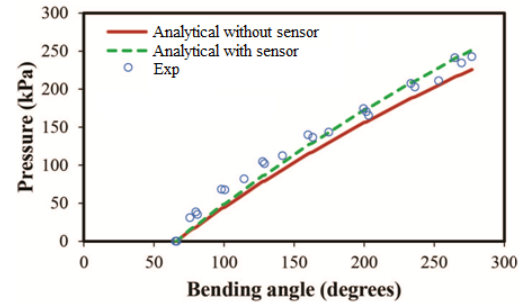


Fig. 7. Free space bending results of measured air pressures (Exp), predicted air pressures before and after considering sensor stiffness.

combined using the dimensions of the extension bar to obtain the overall force at the actuator tip regardless of its direction.

The material properties μ_t , μ_b , and μ_s for the analytical model were determined by calibration. Three actuators were used in this study, with the same actuator design and the same material for their top and bottom walls, therefore we used $\mu_t = \mu_b = \bar{\mu}$. The same calibration procedure was followed to obtain the averaged material property $\bar{\mu}$ as presented previously in [40]. Despite using a different actuator design of $(a, b, t, L) = (6, 2, 2, 170)$ mm, the calibration resulted in a very similar $\bar{\mu} = 0.313$ MPa with those of [40], mainly due to the same wall thickness and material combination used in both designs. The same calibration procedure was used again to estimate the sensor stiffness $\mu_s = 0.103$ Nm/rad, using the same group of actuators bending in free space with/without the bend sensor. The estimated material properties were used in all experiments.

B. Free-space bending test

In the free-space bending test, the pressure-angle relationship of (4.18) is validated. The effect of integrating a bend sensor into the actuator is also accessed by comparing the results of (4.18) with or without sensor stiffness μ_s . In the experimental

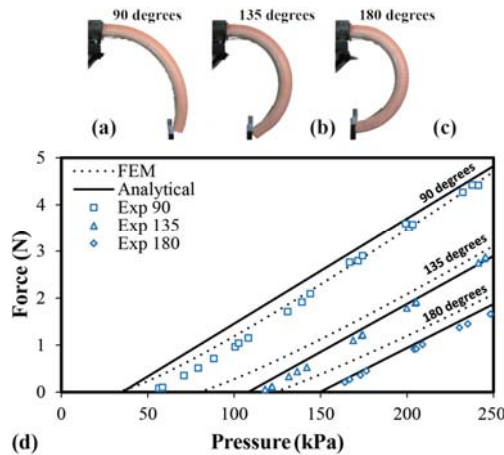


Fig. 8. Isometric test results. (a)-(c) actuator bending for 90, 135, 180 degrees, (d) comparison of analytical model, FEM, and experimental (Exp) results.

setup, an actuator was mounted horizontally on the platform, with the distal tip bending downwards in the vertical plane without obstacles. Without rigid structural support, the mounted actuator exhibited a 60-degree downwards natural bending angle due to gravity.

Three trials were conducted, and for each trial the actuator was pressurized from its natural resting position with air pressure increased from 0 to 250 kPa, and actuator bending angles were measured by the integrated bend sensor.

To validate the analytical model of (4.18), the measured bending angles were used to calculate air pressure, and compare with the actual supplied air pressure values. To illustrate the influence of the integrated bend sensor, two pressure estimations were made by setting $\mu_s = 0$ and $\mu_s = 0.103 \text{ Nm/rad}$, respectively. They are compared in Fig. 7 against the measured air pressure (Exp). The analytical model was derived based on internal material stretch, which should be zero at the natural resting condition. Therefore, the 60 degree initial bending angle was subtracted from sensor measurements before applying the analytical model. Similar procedures were conducted in other tests where the analytical model was used. In the results shown in Fig. 7, the estimated pressure values match those obtained experimentally throughout the actuator bending range. Moreover, considering the sensor stiffness results in a noticeably better match to the experimental measurements with a standard deviation of $\sigma=12.5\text{kPa}$, or 5.0% of the full pressure range of 250kPa, comparing with $\sigma=18.9\text{kPa}$ (7.6%) when sensor stiffness is not considered. The calibration result of $\mu_s = 0.103 \text{ Nm/rad}$ was therefore justified and used in the rest of this study.

Actuator hysteresis is a well-known issue for linear PAM actuators, which is generally accepted to be caused by the friction of fiber braiding and between different layers of materials within the actuator [6]. However, although our actuator design utilizes a fiber layer, there is minimum sliding between the fiber and the actuator body, and hence the friction loss is negligible during actuation. Therefore the dominating internal interaction is material stretch, which does not lead to hysteresis, as observed in previous work on soft bending actuators made from the same soft material [34]. In our previous experiments with the same actuator design, no significant

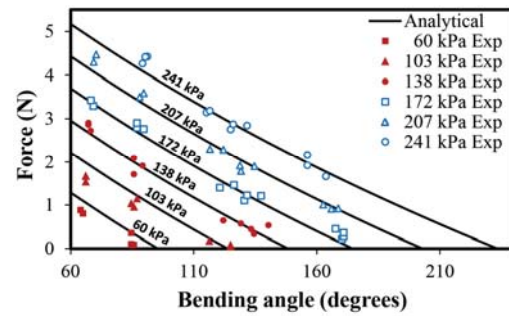


Fig. 9. Isotonic test results. Comparison of force predictions from the analytical force model (Analytical) and experimental force measurements (Exp).

hysterical effect was observed [40], therefore hysteresis is not investigated in this study.

C. Isometric test

In an isometric test, the actuator was constrained at constant bending angles while input pressure increased from 0 to 250kPa. In each state the contact forces were measured by the force sensor. The experiment consisted of three trials, with three actuator positions considered for each trial: 90, 135, and 180 degrees (without subtracting the natural resting angle), as shown in Fig. 8(a)-Fig. 8(c). The analytical model was used to estimate bending forces using the measured bending angles. Comparatively, FEM simulations were conducted following the same experimental procedure and bending angles.

The calculated forces from the analytical and FEM models are compared with the experimental force measurements in Fig. 8(d). The analytical results form parallel lines for each bending angle. This trend is matched by the FEM and experimental results, with FEM results exhibiting increasing deviations at larger bending angles, possibly caused by large material strains and hence FEM element deformations. The experimental measurements are closely matched by the analytical results with a standard deviation of $\sigma=0.26 \text{ N}$ (6.0% of a maximum force of 4.4 N) for 90 degrees, $\sigma=0.13 \text{ N}$ (4.6% of 2.83 N) for 135 degrees, and $\sigma=0.12 \text{ N}$ (5.6% of 2.1 N) for 180 degrees.

D. Isotonic test

In the isotonic test, the input pressure was kept at a range of constant values, and interaction forces were measured at different bending angles. Similar with the previous experiments, force predictions from the analytical model were compared with measured forces.

The experimental results are shown in Fig. 9, where each trial forms an isotonic line that intersects with both axes. The intersections with the horizontal axis indicate the maximum bending angle for the particular input pressure where force drops to zero. The intersections with the vertical axis indicate the maximum achievable force for that pressure, which occurs at zero bending. Between the two intersections, the force-angle relationship is nonlinear as described in (4.18). This nonlinearity is introduced by the hyperelastic material property and therefore captured very well by the analytical model. The comparison results for each pressure configuration are listed in TABLE I. The analytical model provides a better estimation for larger pressures, with 2.7% average error for 241kPa, comparing with 16.1% for 60kPa. This is mainly due to the

TABLE I
Comparison between Analytical Force Estimations and Experimental Measurements for Isotonic Test Results

Pressure (kPa)	F_{\max} (N)	σ (N)	σ/F_{\max}
60	1.3	0.21	16.1%
103	2.2	0.24	10.9%
138	3.0	0.13	4.3%
172	3.7	0.15	4.1%
207	4.4	0.18	4.1%
241	5.2	0.14	2.7%

F_{\max} is the maximum force at the corresponding pressure setting

complex actuation procedure the actuator underwent not fully considered in the analytical model, such as interactions between different material layers, nonlinear bulging and deformations on radial and circumferential directions. The above factors were more significant for lower pressures, where the actuator started deforming from its original state. Although an averaged material shear modulus was used to incorporate the above factors, the calibration process for the shear modulus resulted in an optimal value for the entire pressure range from 0 to 250kPa. Therefore, the resulting analytical model provided better predictions for higher pressures. The isotonic test results also illustrated the compliant feature of soft bending actuators, where each isotonic line in Fig. 9 gave a quantitative measure of how much the actuator would deform with an exerted force.

VI. CONCLUSIONS AND FUTURE WORK

This work demonstrated that the bending and tip-force capabilities of the soft fiber-reinforced bending actuators under quasi-static conditions could be characterized, modeled, and controlled. Moreover it was shown that integrating an off-the-shelf bend angle sensor to the actuator could provide force estimation without requiring a dedicated force sensor. This is a critical step to demonstrate the capability of soft bending actuators for robotic applications. Although the study assumed quasi-static states with slow motions, its conclusions are applicable to most application scenarios where soft actuators have advantages, ranging from manipulating unmodeled/fragile objects to interacting with unstructured environments, where compliance, adaptability and safety are more critical concerns than actuation speed and high bandwidth.

An analytical model was developed to describe the force generation mechanism and quantify the relationship between the input pressure, bending angle and tip bending force. The resulting force model consists only of polynomial functions, therefore it can be easily embedded onto a micro controller for real-time calculation and control in robotic applications. The effect of the reinforcement fiber layer was also investigated. A geometrical study was conducted for the actuator on the influence of different fiber pitch angles on actuator geometry. To validate the analytical models, a FEM model of the actuator was developed closely resembling the real actuator. In the comparison results, the FEM simulation could provide a closer match to the reality, while compromising real-time capability.

In addition, the FEM model also highlighted the critical regimes of stress concentration in the internal structures.

Actuators were fabricated and tested to validate the analytical and FEM models in free-space, isometric, and isotonic experiments. The results demonstrated that the analytical model was able to capture the relationship between input pressure, bending angle, and the output bending force at the actuator tip with good accuracy, despite the approximations and linearization during the modeling process. In addition, the proposed analytical model provided a direct computational link between an actuator design and its performance, hence the parameters of an actuator design could be calculated from a given performance criteria, simplifying the design iteration and hence reducing the time and cost. Potential applications include glove-type wearable robotic devices where interaction forces are mostly encountered at the actuator tip [10, 23], and new actuator designs featuring the same topology.

In future work, analytical modeling of nonlinear actuator behaviors, such as non-uniform bending and radial bulging will be tackled. Viscoelastic effect, air compressibility and heat dissipation arising from fast actuation will be investigated to analyze the dynamic actuator behaviors. Distribution of interaction forces along the actuator body will be investigated, together with engineering aspects such as actuator fatigue and failure modes. The modeling approach could be generalizable to other actuator designs following the same fundamental structure of a single air-chamber and fiber reinforcements. Applications of soft bending actuators will be carried out exploring the integrated bending sensor, in scenarios such as contact detection and force control. Through modeling analysis and experimental validations, the static and dynamic properties of the actuators could be demonstrated to the robotics research community. With its unique features and the tools for analysis, design, and control, soft bending actuator will be a capable competitor of rigid-bodied actuators for robotic applications.

REFERENCES

- [1] Haddadin, S., Albu-Schaffer, A. and Hirzinger, G. (2009). Requirements for Safe Robots: Measurements, Analysis and New Insights. *The International Journal of Robotics Research*, 28: 1507-1527.
- [2] Doulgeri, Z. and Fasoulas, J. (2003). Grasping control of rolling manipulations with deformable fingertips. *Mechatronics, IEEE/ASME Transactions on*, 8(2), 283-286.
- [3] Kim, S., Laschi, C. and Trimmer, B. (2013). "Soft robotics: a bioinspired evolution in robotics", *Trends in biotechnology*, vol. 31, no. 5, pp. 287-294.
- [4] Majidi, C. (2013). "Soft Robotics: A Perspective—Current Trends and Prospects for the Future," *Soft Robotics*, vol. 1, pp. 5-11.
- [5] Chen, F. J., Dirven, S., Xu, W. L., and Li, X. N. (2014). Soft actuator mimicking human esophageal peristalsis for a swallowing robot. *Mechatronics, IEEE/ASME Transactions on*, 19(4), 1300-1308.
- [6] Daerden, F. and Lefeber, D. (2002). Pneumatic artificial muscles: actuators for robotics and automation, *European journal of Mechanical and Environmental Engineering*, 47(1): 11–21, 2002.
- [7] Wait, K. W. and Goldfarb, M. (2014). A pneumatically actuated quadrupedal walking robot. *Mechatronics, IEEE/ASME Transactions on*, 19(1), 339-347.
- [8] Riachy, S. and Ghanes, M. (2014). A nonlinear controller for pneumatic servo systems: Design and experimental tests. *Mechatronics, IEEE/ASME Transactions on*, 19(4), 1363-1373.
- [9] Yao, J., Jiao, Z., Ma, D., and Yan, L. (2014). High-accuracy tracking control of hydraulic rotary actuators with modeling uncertainties. *Mechatronics, IEEE/ASME Trans on*, 19(2), 633-641.

- [10] Polygerinos, P., Wang, Z., Galloway, K.C., Wood, R.J., and Walsh, C.J. (2015). Soft robotic glove for combined assistance and at-home rehabilitation, *Robotics and Autonomous Systems*, vol13: 135–143, 2015.
- [11] Wang, F.J., Liang, C.M., Tian, Y.L., Zhao, X.Y., and Zhang, D.W. (2014) Design of a piezoelectric-actuated microgripper with a three-stage flexure-based amplification, *IEEE/ASME Transactions on Mechatronics*, DOI: 10.1109/TMECH.2014.2368789, 2014.
- [12] Liang, C.M., Wang, F.J., Tian, Y.L., Zhao, X.Y., Zhang, H.J., Cui, L.Y., Zhang, D.W., and Ferreira, P. (2015). A novel monolithic piezoelectric actuated flexure-mechanism based wire clamp for microelectronic device packaging, *Review of Scientific Instruments*, 2015, 86, 045106.1-11.
- [13] Wang, F.J., Ma, Z.P., Gao, W.G., Zhao, X.Y., Tian, Y.L., Zhang, D.W., and Liang, C.M. (2015). Dynamic modeling and control of a novel XY positioning stage for semiconductor packaging, *Transactions of the Institute of Measurement and Control*, 2015, 37(2): 177-189.
- [14] Li, Y.M. and Xu, Q.S. (2012). Design and robust repetitive control of a new parallel-kinematic XY piezostage for micro/nanomanipulation, *IEEE/ASME Trans. Mechatronics*, vol. 17, no. 6, pp. 1120–1132.
- [15] Roche, E., Wohlfarth, R., Overvelde, J.T.B., Vasilyev, N., Pigula, F., Mooney, D., Bertoldi, K. and Walsh, C. (2014). A bioinspired soft actuated material, *Advanced Materials*, 26(8), 1200-1206.
- [16] Caldwell, D., Tsagarakis, N., Badihi, D. and Medrano-Cerda, G.A. (1998). Pneumatic Muscle Actuator Technology a light weight power system for a Humanoid Robot, *Proceedings of International Conference on Robotics & Automation (ICRA)*: 3053-3058.
- [17] Takuma, T. and Hosoda, H. (2006). Controlling the Walking Period of a Pneumatic Muscle Walker, *The International Journal of Robotics Research*, 25:861-866.
- [18] Rothling, F., Haschke, R., Steil, J. and Ritter, H. (2007). Platform portable anthropomorphic grasping with the bielefeld 20-DOF shadow and 9-DOF TUM hand, *IEEE/RSJ International Conference on Intelligent Robots and Systems (IROS)*: 2951-2956.
- [19] Chou, P. and Hannaford, B. (1996). Measurement and modeling of McKibben pneumatic artificial muscles. *IEEE Transactions on Robotics and Automation*, 12(1): 90-102.
- [20] Tondou, B. and Lopez, P. (2000). Modeling and control of McKibben artificial muscle robot actuators. *IEEE Control Systems Magazine*, 20(2):15–38.
- [21] Davis, S., Tsagarakis, N., Canderle, J., and Caldwell, D. G. (2003). Enhanced modeling and performance in braided pneumatic muscle actuators. *International Journal of Robotics Research*, 22: 213–227.
- [22] Galloway, K., Polygerinos, P., Walsh, C. and Wood, R. (2013). Mechanically Programmable Bend Radius for Fiber-Reinforced Soft Actuators, *International Conference on Advanced Robotics (ICAR)*.
- [23] Polygerinos, P., Lyne, S., Wang, Z., Mosadegh, B., Whitesides, M. and Walsh, C. (2013). Towards a Soft Pneumatic Glove for Hand Rehabilitation, *IEEE/RSJ International Conference on Intelligent Robots and Systems (IROS) 2013*.
- [24] Chen, Z., Shatara, S., and Tan, X. (2010). Modeling of biomimetic robotic fish propelled by an ionic polymer-metal composite caudal fin. *Mechatronics, IEEE/ASME Transactions on*, 15(3), 448-459.
- [25] Wakimoto, S., Ogura, K., Suzumori, K. and Nishioka, Y. (2009). Miniature Soft Hand with Curling Rubber Pneumatic Actuators, *IEEE International Conference on Robotics and Automation (ICRA)*: 556-561.
- [26] Konishi, S., Nokata, M., Jeong, O., Kusuda, S., Sakakibara, T., Kuwayama, M. and Tsutsumi, H. (2006). Pneumatic Micro Hand and Miniaturized Parallel Link Robot for Micro Manipulation Robot System, *IEEE International Conference on Robotics and Automation (ICRA)*: 1036-1041.
- [27] Bishop-Moser, J., Krishnan, G., Kim, C. and Kota, S. (2012). Design of Soft Robotic Actuators using Fluid-filled Fiber-Reinforced Elastomeric Enclosures in Parallel Combinations, *IEEE/RSJ International Conference on Intelligent Robots and Systems (IROS)*: 4264-4269.
- [28] Zhang, L., Bao, G., Yang, Q., Ruan, H. and Qi, L. (2006). Static Model of Flexible Pneumatic Bending Joint, *9th IEEE International Conference on Control, Automation, Robotics and Vision*: 1-5.
- [29] Deimel, R. and Brock, O. (2014). A novel type of compliant, underactuated robotic hand for dexterous grasping, *Robotics: Science and Systems*, pp. 1687-1692.
- [30] Suzumori, K., Endo, S., Kanda, T., Kato, N. and Suzuki, H. (2007). A Bending Pneumatic Rubber Actuator Realizing Soft-bodied Manta Swimming Robot, *IEEE International Conference on Robotics and Automation (ICRA)*: 4975-4980.
- [31] Correll, N., Onal, C., Liang, H., Schoenfeld, E. and Rus, D. (2010). Soft Autonomous Materials - Using Programmed Elasticity and Embedded Distributed Computation. In: *Oussama Kahtib, Vijay Kumar, Gaurav Sukhatme (Ed.): International Symposium on Experimental Robotics (ISER). Springer Tracts in Advanced Robotics*, 2010.
- [32] Morin, S., Shepherd, R., Kwok, S., Stokes, A., Nemiroski, A. and Whitesides, G. (2012). Camouflage and Display for Soft Machines, *Science*, 337: 828-832.
- [33] Ilievski, F., Mazzeo, A., Shepherd, R., Chen, X. and Whitesides, G. (2011). Soft Robotics for Chemists, *Angewandte Chemie*, 123(8): 1930-1935.
- [34] Mosadegh, B., Polygerinos, P., Keplinger, C., Wennstedt, S., Shepherd, R. F., Gupta, U., Shim J., Bertoldi K., Walsh C.J., and Whitesides, G. M. (2014). Pneumatic networks for soft robotics that actuate rapidly, *Advanced Functional Materials*, 24(15), 2163-2170.
- [35] Faudzi, A., Razif, M.R., Nordin, I.N., Suzumori, K., Wakimoto, S. and Hirooka, D. (2012). Development of Bending Soft Actuator with Different Braided Angles, *The IEEE/ASME International Conference on Advanced Intelligent Mechatronics*: 1093-1098.
- [36] Webster, R. and Jones, B. (2010). Design and Kinematic Modeling of Constant Curvature Continuum Robots: A Review, *The International Journal of Robotics Research*, 29(13): 1661-1683.
- [37] Song, Y., Sun, Y., van den Brand, R., von Zitzewitz, J., Micera, S., Courtine, G. and Paik, J. (2013). Soft Robot for Gait Rehabilitation of Spinalized Rodents, *IEEE/RSJ International Conference on Intelligent Robots and Systems (IROS) 2013*.
- [38] Deng, M., Wang, A., Wakimoto, S. and Kawashima, T. (2011). Characteristic Analysis and Modeling of a Miniature Pneumatic Curling Rubber Actuator, *International Conference on Advanced Mechatronic Systems*: 534-539.
- [39] Kelasidi, E., Andrikopoulos, G., Nikolakopoulos, G. and Manesis, S. (2012). A Survey on Pneumatic Muscle Actuators Modeling, *Journal of Energy and Power Engineering*, 6: 1442-1452.
- [40] Polygerinos, P., Wang, Z., Overvelde, J.T.B., Galloway, K., Wood, R., Bertoldi, K., and Walsh, C. (2015). Modeling of Soft Fiber Reinforced Bending Actuators. *IEEE Transactions on Robotics*, 31(3): 778 – 789.
- [41] Yeoh, O. (1993). Some Forms of the Strain Energy Function for Rubber, *Rubber Chemistry and Technology*, 66(5): 754-771.
- [42] Ogden, R. W. (1997). Non-linear elastic deformations: *Courier Dover Publications*, 1997.



Zheng Wang (M'10, SM'16) received the BSc from Tsinghua University (China), MSc with distinction from Imperial College (UK), and PhD with merit from Technische Universität München (Germany). He was a postdoctoral research fellow in Nanyang Technological University (Singapore) between 2010 and 2013, and a postdoctoral fellow with the School of Engineering and Applied Sciences and the Wyss Institute of Bioinspired Engineering at Harvard University between 2013 and 2014. Since July 2014 he has been an Assistant Professor in the Department of Mechanical Engineering at the University of Hong Kong. His research interest include: soft robotics, underwater robots, medical robots, and human-robot interaction.



Panagiotis Polygerinos (M'11) received the B.Eng. degree (top of his class) in mechanical engineering from the Technological Educational Institute of Crete, Heraklion, Greece in 2006, the M.Sc. (with distinction) degree in mechatronics and Ph.D. in mechanical engineering/medical robotics from King's College London, London, U.K., in 2007 and 2011, respectively. From 2012 until 2015, he was a postdoctoral fellow of technology development with the Harvard Biodesign Lab and the Wyss Institute for Biologically Inspired Engineering at Harvard University. He is currently an Assistant Professor with the Ira A. Fulton Schools of Engineering at Arizona State University, USA. His research interests focus on the realization of tasks that are essential to the design, implementation and integration of novel robotic systems and mechatronic devices that improve patient care and human activity.



Johannes T. B. Overvelde received his BSc and MSc (both with distinction) in Mechanical Engineering from Delft University of Technology, the Netherlands in 2012. Currently, he is an Applied Mathematics PhD candidate in Katia Bertoldi's group at the School of Engineering and Applied Sciences at Harvard University. His research interests are in the field of nonlinear structural optimization and computational mechanics.



Kevin C. Galloway received his B.S.E. and Ph.D. in mechanical engineering from the University of Pennsylvania and is currently a research assistant professor in mechanical engineering and the Director of Making at Vanderbilt University. His current research interests include new approaches to design, rapid prototyping from the micro- to the macro-scale, active soft materials, and the manufacture and control of wearable robotic devices.



Katia Bertoldi received her master's degrees from Trento University (Italy) in 2002 and from Chalmers University of Technology (Sweden) in 2003, majoring in Structural Engineering Mechanics. Upon earning a Ph.D. degree in Mechanics of Materials and Structures from Trento University, in 2006, Katia joined as a PostDoc the group of Mary Boyce at MIT. In 2008 she moved to the University of Twente (the Netherlands) where she was an Assistant Professor in the faculty of Engineering Technology. In January 2010 Katia joined as Associate Professor of Applied Mechanics the School of Engineering and Applied Sciences at Harvard University and established a group studying the mechanics of materials and structures.



Conor J. Walsh received his B.A.I and B.A. degrees in Mechanical and Manufacturing engineering from Trinity College Dublin, Ireland in 2003 and an M.S. degree and Ph.D. in Mechanical Engineering from the Massachusetts Institute of Technology in 2006 and 2010 with a minor in entrepreneurship through the Sloan School of Management and also a Certificate in Medical Science through the Harvard-MIT Division of Health Sciences and Technology. During his time at MIT, he had received the Whitaker Health Sciences Fund Fellowship as well as numerous other design, entrepreneurship and mentoring awards. He is an Associate Professor in the Harvard School of Engineering and Applied Sciences and a core faculty member at the Wyss Institute for Biologically Inspired Engineering at Harvard University. His research efforts are at the intersection of science, engineering and medicine with a focus on developing smart medical devices for diagnostic, therapeutic, and assistive applications.